eNeuro

Research Article: New Research - Non-Double-Blind | Sensory and Motor Systems

Transition from Target to Gaze Coding in Primate Frontal Eye Field During Memory Delay and Memory-Motor Transformation

Visual-memory-motor transformations in FEF

Amirsaman Sajad[1,2,3], Morteza Sadeh[1,3,4], Xiaogang Yan[1], Hongying Wang[1] and John Douglas Crawford[1,2,3,4,5]

[1]*Centre for Vision Research, York University, Toronto, Ontario M3J 1P3, Canada*
[2]*Neuroscience Graduate Diploma Program, York University, Toronto, Ontario M3J 1P3, Canada*
[3]*Department of Biology, York University, Toronto, Ontario M3J 1P3, Canada*
[4]*School of Kinesiology and Health Sciences, York University, Toronto, Ontario M3J 1P3, Canada*
[5]*Department of Psychology, York University, Toronto, Ontario M3J 1P3, Canada*

DOI: 10.1523/ENEURO.0040-16.2016

Received: 25 February 2016

Accepted: 23 March 2016

Published: 5 April 2016

Funding: Canadian Institutes of Health Research (CIHR): MOP 130444. Ontario Graduate Scholarship; Queen Elizabeth II Scholarship; Provost Dissertation Award;

Conflict of Interest: Authors report no conflict of interests.

A.S. and J.D.C. designed research; A.S., M.S., X.Y., and H.W. performed research; A.S. analyzed data; A.S., M.S., X.Y., H.W., and J.D.C. wrote the paper.

Corresponding Author: Prof. J.D. Crawford, Centre for Vision Research, Room 0009A LAS, 4700 Keele Street, Toronto, Ontario M3J 1P3, Canada. Email:jdc@yorku.ca

Cite as: eNeuro 2016; 10.1523/ENEURO.0040-16.2016

Transition from Target to Gaze Coding in Primate Frontal Eye Field During Memory Delay and Memory-Motor Transformation

Abbreviated Title: visual-memory-motor transformations in FEF

Authors: Amirsaman Sajad[1-3], Morteza Sadeh[1,3,4], Xiaogang Yan[1], Hongying Wang[1], and John Douglas Crawford[1-5]

[1]Centre for Vision Research,
[2]Neuroscience Graduate Diploma Program,
[3]Department of Biology,
[4]School of Kinesiology and Health Sciences,
[5]Department of Psychology,
York University, Toronto, Ontario, Canada, M3J 1P3,

Author Contributions: AS and JDC designed research; AS, MS, XY, and HW performed research; AS analyzed data; AS and JDC wrote paper; All reviewed paper.

Corresponding Author:
Name: Prof. J.D. Crawford
Address: Centre for Vision Research, Room 0009A LAS
4700 Keele Street, Toronto, Ontario, M3J 1P3;
Telephone: 416-7362100, ext: 88621
Email: jdc@yorku.ca

Number of pages: 71 (full manuscript, excluding title page)
Number of Figures: 11
Number of words for Abstract: 247
Number of words for Significance Statement: 119
Number of words for Introduction: 743
Number of words for Discussion: 1822

Acknowledgements: The authors thank Ms. S. Sun and Dr. Gerald Keith for computer programming assistance, and Drs. S. Dash and R. Marino for editorial comments.

Conflict of interest: Authors report no conflict of interests

Funding Sources:
This study was supported by a grant from the Canadian Institutes for Health Research to J.D. Crawford. J.D. Crawford was supported by the Canada Research Chair Program. A. Sajad was supported by an Ontario Graduate Scholarship, a Queen Elizabeth Scholarship, and a York Provost Dissertation Award. M. Sadeh was supported by an Ontario Graduate Scholarship.

Abstract

The Frontal Eye Fields (FEF) participate in both working memory and sensorimotor transformations for saccades, but their role in integrating these functions through time remains unclear. Here, we tracked FEF spatial codes through time using a novel analytic method applied to the classic memory-delay saccade task. Three-dimensional recordings of head-unrestrained gaze shifts were made in two monkeys trained to make gaze shifts toward briefly flashed targets after a variable delay (450-1500 ms). A preliminary analysis of visual and motor response fields in 74 FEF neurons eliminated most potential models for spatial coding at the neuron population level, as in our previous study (Sajad et al., 2015). We then focused on the spatiotemporal transition from an eye-centered target code (*T*; preferred in the visual response) to an eye-centered intended gaze position code (*G*; preferred in the movement response) during the memory delay interval. We treated neural population codes as a continuous spatiotemporal variable by dividing the space spanning *T* and *G* into intermediate *T-G* models and dividing the task into discrete steps through time. We found that FEF delay activity, especially in visuomovement cells, progressively transitions from *T* through intermediate *T-G* codes that approach, but do not reach, *G*. This was followed by a final discrete transition from these intermediate *T-G* delay codes to a 'pure' *G* code in movement cells without delay activity. These results demonstrate that FEF activity undergoes a series of sensory-*memory*-motor transformations, including a dynamically evolving spatial memory signal and an imperfect memory-to-motor transformation.

Significance Statement

Gaze-related signals in frontal cortex are often used as an experimental model for visual working memory. However, the spatial codes employed during the delay between target-related visual activity and intended gaze-related motor activity remain unknown. Here, we show that frontal eye field delay activity (particularly in visuomovement neurons) shows a progressive transition through intermediate target-gaze codes, with a further jump to coding intended gaze position in movement neurons with no delay response. Since our analytic method is based on fitting neural activity against variable behavioral errors, this suggests that such errors accumulate during the memory delay, and further escalate during the final memory-to-motor transformation. Any of these vulnerable processes might be further degraded by diseases that affect frontal cortex.

Introduction

Primates routinely use remembered stimuli to guide spatial behavior, with varying degrees of spatial precision (Gnadt et al., 1991; White et al., 1994). This could involve a sensory-to-memory transformation, maintenance of the target in working memory, and a memory-to-motor transformation (Goldman-Rakic, 1987; Postle, 2006; Bays et al., 2011; Chatham and Badre, 2015). However, it is not known at what point in this sequence the *spatial* code for the sensory stimulus is transformed into a spatial code for movement, and likewise, when and how spatial errors in behavior arise (Gnadt et al., 1991; Stanford and Sparks, 1994; Krappmann, 1998; Opris et al., 2003; Faisal et al., 2008).

Memory-guided saccades provide an ideal experimental model for this question because many saccade-related neurons in the brainstem and cortex exhibit spatially-selective visual, memory, and / or movement responses (Funahashi et al., 1989; Bruce and Goldberg, 1985; Schall, 2015; Wurtz et al., 2001). Further, the gaze control system, which normally controls both eye and head motion, provides convenient parameters for spatial coding (i.e., target, gaze, eye, head) in various egocentric frames (eyes, head, or body) (Freedman and Sparks, 1997; Martinez-Trujillo et al., 2003; Sajad et al., 2015). Still, a complete description of the spatiotemporal transformations in the sensory-memory-motor transformation for gaze control remains elusive.

Neurophysiological studies often trained monkeys to look toward a location that is spatially incongruent with the visual stimulus in order to dissociate target (*T*) coding in visual responses vs. intended gaze position (*G*) coding in motor responses, without

addressing the intervening memory delay (Gottlieb and Goldberg, 1999; Everling and Munoz, 2000; Sato and Schall, 2003). Most studies that explored this issue during delay activity employed similar tasks to look for a discrete target-to-gaze switch (Funahashi et al., 1993; Mazzoni et al., 1996; Zhang and Barash, 2004). Other studies showed a gradual rotation of the population direction vector from the stimulus toward the instructed movement direction in Dorsolateral Prefrontal Cortex (dlPFC), or a more abrupt rotation in the mediodorsal thalamus (Takeda and Funahashi, 2004; Watanabe et al., 2009). However, no previous experiment tested if delay activity evolves across time through intermediate spatial codes (i.e., between *T* and *G*) in the visual-memory-motor transformations for saccades *toward* remembered stimuli.

Assuming that one could track such codes through time, there are several ways that a *T*-*G* transition could occur in memory-guided saccades (Fig. 1*D*). A sustained *T* code followed by a late *T*-*G* transition would be compatible with sensory theories of working memory (Funahashi et al.,1993; Constantinidis et al., 2001), whereas an early *T*-*G* transition would be compatible with motor theories of working memory (Gnadt and Andersen, 1988; Gaymard et al., 1999; Curtis and D'Esposito, 2006; Rainer et al., 1999). Alternatively, *T*-*G* transition could progressively accumulate during the delay (Gnadt et al., 1991; Wimmer et al., 2014). Another possibility (not shown) is that there is no transition of coding *within* any given population of cells, but rather a temporal transition of activity from a *T*-tuned population of neurons to a *G*-tuned population (Takeda and Funahashi, 2007).

The monkey frontal eye fields (FEF), located in prefrontal cortex, are an ideal location to study this question because they are directly involved in the sensorimotor

transformation for saccades and head-unrestrained gaze shifts (Bruce and Goldberg, 1985; Schall, 2015), and are part of the working memory network (Funahashi et al., 1989; O'Sullivan et al., 1995; Dias and Segraves, 1999; Sommer and Wurtz, 2001). In a recent study we exploited the variable behavior of head-unrestrained gaze shifts to show that FEF visual and motor responses encode *T* and *G* respectively (both relative to initial eye orientation) in saccades made toward remembered visual stimuli (Sajad et al., 2015). However, this previous analysis could not show when or how this transition happens, and did not explore the contributions of individual cell types. Here, we used a similar approach, but applied our analysis in steps through time to fit a continuum of intermediate *T-G* models through the entire course of a memory-guided saccade task. Since this method is based on fitting spatial models against variable behavior such as errors in final gaze direction (Keith et al., 2009; Sajad et al., 2015), this also provided a direct measure of how such errors accumulate through different phases of a memory-guided gaze shift. Further, with the use of a larger data set, we were able to categorize our cells into different memory (or non-memory) related populations, in order to understand their differential contributions through time to the *T-G* transition.

Materials and Methods

Surgical procedures, identification of FEF, and behavioral data recordings

All protocols were in accordance with the Canadian Council on Animal Care guidelines on the use of laboratory animals and approved by the York University Animal Care Committee. The data were collected from two female *Macaca mulatta* monkeys (monkeys A and S). Each animal underwent surgeries for implanting the recording chamber (19mm diameter) which was centered in stereotaxic coordinates at 25mm anterior for both monkeys, and 19mm for one and 20mm lateral for the other. A recording chamber was attached over the trephination with dental acrylic (Fig. 2). In order to eliminate non-viable spatial models of neural coding from our analysis (see below), we needed to record head-unrestrained gaze shifts in three dimensions (3-D). To do this, two 5-mm-diameter sclera search coils were implanted in one eye of each animal and two orthogonal coils mounted on the head (Crawford et al., 1999).

Behavioral paradigm

Monkeys were trained to perform the classic memory-guided gaze task in completely head-unrestrained conditions (Fig. 1*A*). After fixating a visual stimulus presented on the screen, a second visual stimulus (target) briefly flashed for 80-100ms in the periphery cuing the gaze shift goal. However, the animal had to withhold gaze until the instruction to make gaze shift (Go-signal = disappearance of fixation target) was provided, at which time a gaze shift was made to the remembered location of the target. The Go-signal was presented at a random time within a flat distribution that ranged 450-850ms (for 56/74 neurons) or 700-1500ms (for 18/74 neurons). Animals were allowed a relatively large reward window of 5-12° in radius (visual angles) around the target. If the animal

kept gaze stable in the reward window for at least 200ms after the gaze shift, a juice reward was provided. Visual stimuli were laser-projected on a flat screen, positioned 80cm away from the subject.

Our large reward window allowed animals to produce natural (untrained) errors in final gaze direction (Fig. 1*B*). The variable component of these errors was necessary to dissociate the most important models (i.e., target and gaze models) described below. To quantify these we first calculated systematic gaze errors by computing the parameters of the function [dG = a1 dT + a2], separately for vertical and horizontal components, where dG was gaze displacement and dT was target displacement from initial gaze position. This revealed hypometria and vertical/horizontal offsets consistent with previous studies of memory-guided saccades (De Bie et al., 1987; White et al., 1994). Variable errors were quantified as the remaining errors that were unexplained by the systematic errors (i.e., residuals of the linear fit). Variable errors in behavior were distributed normally with SD in x-direction (SDx)= 6.2, and in y-direction (SDy) = 5.8 for animal S, and SDx = 5.9 and SDy = 5.7 for animal A. The average magnitude of the variable errors (mean ± SD) was 6.3 ± 6 degrees. As we shall see, these values were sufficient to statistically separate our target and gaze models, as were other variations in 3-D eye and head orientation for the other models tested (Sajad et al., 2015).

Extracellular Recording Procedures

Extracellular activity from single FEF neurons was recorded using tungsten microelectrodes (0.2-2.0 MΩ impedance, FHC). The neural signal was amplified, filtered, and stored with the Plexon MAP system for offline cluster separation using principal component analysis with the Plexon Offline sorter software. The recorded sites

were considered to be within the FEF if microstimulation with a current <50 μA (70ms trains of monophasic pulses; 300μs/pulse, generated with a frequency of 300Hz) evoked a saccade while the head was restrained (Fig. 2*B;* Monteon et al., 2010; 2012; 2013)

The search for neuron was conducted when the animal was freely scanning the environment in a lighted room with the head free to move. When a neuron with clear and stable spiking was isolated, the experiment began. A rough estimate of the neuron's RF was first obtained using memory-guided gaze shifts to a wide spread of targets presented one at a time from a central fixation point. Then an array of gaze targets were set to cover the neuron's RF including the flanks of the RF (Fig. 1*B*, gray dots). Targets were positioned in a rectangular array (ranging between 4×4 to 8×8, 5-10° apart depending on the size and shape of the RF). Initial fixation positions were randomized within a central window with width ranging from 10-40° in proportion with the estimated size of the RF (example shown in Fig. 1*B*).

Data inclusion criteria (neurons and behavior)

We recorded neuronal activity from over 200 sites in the FEF of the two animals. However, since our method relies on detailed analysis of the RF of single neurons only data from sessions for which we had clear isolation of spiking data were included to eliminate any multi-unit activity from analysis. Also, only neurons for which enough trials were recorded to uniformly cover a decent extent of the RF, and showed either visual or pre-saccadic movement response types (or both) were included in the analysis. After applying our exclusion criteria a total of 77 neurons were used for analysis (57 were

previously analyzed in another study). 3/77 neurons despite having clear visual and / or movement response did not exhibit any spatial tuning and thus were eliminated. So, a total of 74 neurons contributed to the results in this study. The anatomic distribution of these neurons in the recording chambers is shown in Fig. 2*B*.

To obtain the behavioral data, the onset of gaze shift was defined as the time when the gaze (eye in space) velocity exceeded 50°/s and the gaze end-time was marked at the time when velocity declined below 30°/s. Final gaze positions used for spatial analysis were sampled at the gaze end-time. Individual trials were excluded offline if gaze shift was clearly not directed towards the target, or the gaze error exceeded the regression line of gaze error versus retinal error by at least two standard deviations (SD) (errors in gaze end-point scale with gaze shift size). Furthermore, trials in which the subject made an anticipatory gaze shift (with reaction time < 100ms after Go-signal) were eliminated to ensure that animals waited for the go-signal (extinction of the first fixation light) to generate a saccade. In a behavioral analysis based on the same task in the same two monkeys, it was confirmed that saccade onset correlated with the Go-signal (Sadeh et al., 2015). Finally, trials in which the gaze, eye, and head were not stable during the delay period were eliminated (for details see Sajad et al., 2015). After all trial exclusions were applied, on average, 211 trials per neuron were used for analysis.

Neuron classification

We categorized neurons based on the temporal profile of their response (firing rate) during visual, memory, and movement periods. Note that in this experiment each trial was unique both in terms of the starting position and the metrics of the gaze shift and a

large proportion of trials were spatially spread outside of the RF hot-spot, the region where the neuron is most responsive to. Therefore, in order to provide a measure of a neuron's responsiveness we analyzed the activity of the neuron in the 10% of trials in which the neuron was most active (Spk10) which would roughly correspond to trials that fall near the center of the best-fit RF (see next section). Spk10 was calculated for different time periods and used to identify whether a neuron had visual, delay, or movement response as described below.

If Spk10 at 80-180ms after target onset (an early visual period) and/or -50 to +50ms relative to gaze onset (peri-saccadic period) was higher than 25 spikes per second (spk/s) relative to the pre-target baseline we characterized the neuron as having visual and/or movement response (Sajad et al., 2015). A neuron was deemed responsive during delay period if the average of the Spk10 during the 100ms period prior to the presentation of the Go-signal was greater than 15spk/s and was significantly higher than the trial-matched baseline (pre-target) activity levels ($p < 0.05$, Paired-sample Wilcoxon Signed-rank Test). These criteria resulted in a classification similar to that obtained by visual inspection: four classes including 1) visual (V) neurons which did not exhibit movement activity, 2) visuomovement (VM) neurons which exhibited both visual and movement responses, 3) delay-movement (DM) neurons which did not exhibit visual response but showed delay activity prior to the Go-signal, and 4) movement-only (M) neurons which only exhibited a movement response starting after the Go-signal.

Model Fitting Procedures

In order to systematically test between different spatial parameters, we fit spatial models to RF data for every neuron using a procedure that has now been described several times (Keith et al., 2009, DeSouza et al., 2011, Sajad et al., 2015, Sadeh et al., 2015). In brief, the RF of the neuron was plotted by overlaying firing rate data (number of spikes divided by sampling window width for each trial) over two-dimensional position data corresponding to the spatial parameter related to the candidate model, such as target position relative to the eye. The predictability power of the model for the recorded data was quantified by obtaining Predicted Sum of Squares (PRESS) residuals across all trials, which is a form of cross validation used in regression analysis (Keith et al., 2009). Specifically, the PRESS residual for a single trial was obtained by: 1) eliminating that trial from RF data, 2) fitting the remaining data points non-parametrically using Gaussian kernels at various bandwidths (2-15°), and 3) obtaining the residual between the fit and the missing data point. The overall predictability power of the model for the recorded data set was quantified by the average of PRESS residuals across all trials for that neuron. Examples of this process will be described below. Once PRESS residuals of all tested models were obtained the spatial code was defined as the model (using the kernel bandwidth) that yielded the overall best fit to the data.

In a preliminary analysis similar to that of our previous study (Sajad et al., 2015; which used an overlapping but smaller population of neurons) we tested all of the models that have been proposed for egocentric coding in the gaze control system against the visual and movement responses of our neurons (we did not provide allocentric visual cues so such models were not tested). This included models of target location vs. gaze, eye-in-head, and head motion (both final position and displacement) in eye-centered, head-

centered, and body-centered frames of reference, for a total of 11 models (as noted above, most of these tests required the use of 3-D head-unrestrained recordings). Since this replicated our previous analysis on a smaller dataset, but with slightly better statistics, we only summarize the results here.

Target location relative to initial eye orientation (*Te*) was the best model for describing our total population of visual responses, with all other models statistically eliminated (Brown-Forsythe test). Future gaze position relative to initial eye orientation (*Ge*) gave the best overall fit for our total population of motor responses, with all other models statistically eliminated except for eye-in-head displacement and gaze displacement, which were mathematically very similar to *Ge*. Therefore, we used *Te* and *Ge* as the best representatives of visual and motor coding, abbreviated henceforth as simple *T* and *G*. Note that *G* is the visual axis in space controlled by both eye and head motion; this is still head-unrestrained data.

Note that all of these models are correlated with each other to some extent (for example, when the target is on the right, generally gaze, eye, and head move to the right). This is why it has been so difficult to separate them using standard correlation techniques (reviewed in Sajad et al. 2015). An advantage of our method is that it allows each model fit to explain all of the variations in the data that it can (even if these arise from cross-correlation), so that one then statistically compares only the data that the model cannot explain (i.e., the residuals at each point on the RF). For example, to say that *G* is statistically superior to *T* means that including errors in gaze position explains variations that cannot be accounted for by *T*, and a superior fit for *T* means that *G* errors

introduce spatial variability in the fit that is not accounted for in the neural response. However, it is also possible that the ideal fit comes somewhere between *T* and *G*.

The Target-Gaze Continuum

Unlike previous studies, which only made a distinction between *T* and *G* as two possible spatial codes, we also considered intermediary codes between *T* and *G* by creating a quantitative *T-G* continuum between and beyond these spatial models (Fig. 1*D*). This is similar to the notion of intermediate reference frames (Bremner and Andersen, 2014; Blohm et al., 2009; Avillac et al., 2005), but here we are taking intermediate codes for two different variables within the same reference frame (eye coordinates). As described in Sajad et al., (2015) these intermediate spatial models were constructed by dividing the distance between target position and final gaze position for each trial into 10 equal intervals and 10 additional intervals extended on either tail (beyond *T* and *G*). Figure 3*A* shows an example analysis of a visual response sampled from 80 to 180ms after target onset. The RF plots corresponding to three spatial models along the *T-G* continuum are shown in Figure 3A-*2*. In the RF plots, each circle represents firing rate data (diameter) for a single trial plotted over position data corresponding to the tested model (The circles are not shown in other RF plots throughout the paper). The color code represents the non-parametric fit made to all data points (at a kernel bandwidth of 4 degrees, which was the bandwidth that yielded the overall best-fit for this neuron). Below each RF plot, the PRESS residuals for all data points are shown, which provide a measure for the predictability power of the model for the data points. The mean of the PRESS residuals (mean PRESS) provided the overall predictability power of the model for our dataset. 3A-*3* shows mean PRESS (y-axis) as a function of tested spatial model

along the *T*-*G* continuum (x-axis). The model which provides the lowest mean PRESS (marked by red arrow) is the model with the highest predictability power and thus is identified as the spatial code of the neuron. For this example visual response the best-fit model (i.e., spatial code) is the intermediate model one step away from *T* (towards *G*). Note that the RF corresponding to the best-fit model (B, left panel) shows a relatively high degree of *spatial coherence* with high neuronal response spatially confined to a restricted region (red color). The most spatially-coherent fit would be a fit that gives the lowest overall variance in the data relative to each point on the RF, corresponding quantitatively to the lowest residuals of the fit. As the RF representation gets further from the best-fit representation (middle, and right panels) the RF becomes progressively less coherent (as visualized by size-gradient of the circles and the color map), and the magnitude of the PRESS residuals increases.

Time-normalization and activity sampling for spatiotemporal analysis

The specific aims of this study required a new means of analyzing data that we have not described previously: applying our spatial analysis through discrete time-steps spanning the visual, delay, and motor responses of each trial. This proved challenging because we used a variable delay period. In such a paradigm, aligning trials the standard way (with either the visual stimulus or saccade onset) results in the loss and/or mixing of activities across trials, and thus would not allow us to trace spatial coding through the entire trial across all trials (Fig. 3*B*). To overcome this challenge, we normalized the time between an early visual period and movement onset for all trials and applied our analysis method to RFs sampled from the time-normalized activity profile. Our analytic method thus treats time and space similarly, since the spatial codes tested in this study

(i.e., the *T-G* continuum) are also obtained through normalization of errors in behavior (i.e., the vector difference between target position and final gaze position).

In order to sample neuronal activity using the time-normalized scheme, activity was sampled starting from an early visual period, which was the onset of the visual activity (mean = 87ms after target onset) for visually-responsive (V and VM) neurons and 80ms after target onset for neurons with no visual response. The duration between this early visual period and gaze movement onset was on average 895ms (± 234ms, SD) across all trials. For spatiotemporal analysis the firing rate of the neurons (spikes/sec; number of spikes divided by the sampling interval for each trial) was sampled at 16 half-overlapping windows from this time-normalized data. This choice of sampling window numbers was based on the approximate ratio of the duration of the visual response to delay period to movement response including a post-saccadic period starting from gaze onset (visual:delay:movement is approximately 3:10:3).The final (16th) time-step corresponded to an entirely post-saccadic period starting from the onset of gaze shift. Because of the time-normalization process the sampling window width scaled with the duration between visual response onset and movement onset on a trial-by-trial basis. On the 16-step time-normalized scale, the visual burst on average lasted 2.5 steps (SD = 0.81 steps), ending by the end of the third time-step in 94.5% of trials. The presaccadic duration was on average 1.35 steps (SD = 0.67), and for about 90% of the trials started after the beginning of the 14th time-step. Therefore, in the time period interleaving the first three and final three time-steps the sampled activity was largely dominated by delay activity. The sampling window width was on average 119ms

(±37ms, SD) and was no less than 50ms for any trial which ensured enough neuronal spikes captured in the sampling window to perform effective spatial analysis.

Thus, this time-normalization procedure allowed us to consider the entire sequence of visual-memory-motor responses as a continuum. It causes blurring of some other events across trials (e.g., the Go-signal), or mixing of visual and movement responses in the delay period but these possibilities are controlled for in the Results section (see Figure 8).

Testing for spatial selectivity (for single neuron, and population)

Our model-fitting approach would provide us with valid results if the sampled neuronal activity exhibits spatial selectivity. Therefore, we excluded data points both at single neuron level and at population level which did not exhibit significant spatial tuning of any kind.

To test for spatial selectivity for a sampled response for an individual neuron we compared the spatial selectivity of the best-fit representation with its random counterpart. To do this, we randomly shuffled the firing rate data (number of spikes divided by duration of the sampling window) and plotted them over the position data corresponding to the best-fit model, and repeated this procedure 100 times to obtain 100 *random* RFs. The PRESS residuals of these random RFs (and their respective mean PRESS values) were then obtained after fitting the data (non-parametrically, using Gaussian kernels) with the same kernel bandwidth that was used to fit the best-fit model, resulting in a total of 100 mean PRESS residuals. If the mean PRESS residuals for the best-fit model ($PRESS_{best\text{-}fit}$) was at least 2SD smaller than the mean of the

distribution of random mean PRESS residuals (which was normally distributed), then the sampled activity was identified as spatially-selective.

At the population level, even though at a given time-step some neurons exhibited spatial tuning, due to low signal-to-noise ratio or few number of neurons contributing to the population, our estimate for the population code would not be reliable. Therefore, we excluded population data corresponding to time-steps at which the mean spatial coherence of the population was not statistically higher from that of the pre-target baseline which presumably exhibits no spatial tuning (as no task-relevant information is available). The spatial coherence for each neuron contributing to the population spatial coherence was measured using an index:

$$\text{Coherence index} = 1 - \left(\text{PRESS}_{\text{best-fit}} / \text{PRESS}_{\text{random}} \right)$$

Where $\text{PRESS}_{\text{random}}$ provided a measure of the predictability power for the random distribution (average of mean PRESS residuals over the 100 independent distributions). If $\text{PRESS}_{\text{best-fit}}$ was approximately similar to $\text{PRESS}_{\text{random}}$ then coherence index would be a value around 0. Alternatively, if $\text{PRESS}_{\text{best-fit}} = 0$ (which would only occur when the model perfectly accounted for the data) the index would be 1. The coherence index can also be used to determine the amount of variance in the neural data described by the best-fit model. In our data the range of coherence indices was from -0.07 to +0.67. We did not expect coherence index to be 1 especially because neurons in the FEF are shown to be modulated by other non-spatial factors such as attention and reward expectancy (Schall, 2015).

Non-parametric fits to temporal progress of spatial code in single-neurons

The spatiotemporal progression of the neuronal code was analyzed by plotting the best-fit model (y-axis) as a function of the discretely sampled time-steps (x-axis). To visualize these trends (and for the population analysis in the next section) we performed a non-parametric fit to this data for each neuron. Only data corresponding to spatially-tuned time-steps contributed to the fit. Fit values were included for every time-step whose two neighboring time-steps (both before and after) exhibited spatial tuning. The fit was discontinued for the range at which at least two consecutive time-steps were not spatially-tuned. Gaussian kernel with bandwidth of 1 time-step was used for non-parametric fitting of this data. This choice was made conservatively to avoid over-smoothing the data. As can be noted in Figures 5,6,8,9,10, the fit values closely matched the data points obtained for individual neurons. Unless stated otherwise, we used the fit values, rather than individual data points, for statistical tests reported in this study, because they were less likely to be influenced by outliers.

Population analysis and comparison between neuronal sub-populations

Since most theoretical papers suggest that it is neural populations, not individual neurons, that matter most for behavior (Pouget and Snyder, 2000; Blohm et al., 2009), the results presented here focus mainly on our *T-G* analysis of our entire population of neurons as well as several sub-populations (V, VM, DM, M). The overall population coding preference across the *T-G* continuum (continuous trend-lines in Figures 4*E*, 5*B*, 6*B*, 7, 8*B*, 9*B*) at any given time-step was defined as the mean of the fits made to individual neuron data. Since the distribution of spatial code within different neuronal sub-populations did not exhibit a normal distribution, we used non-parametric statistical tests to compare between data across the population, as well as the regression

analyses presented in the Results for VM and DM neurons.

Results

We recorded neurons from over 200 sites in the FEF during head-unrestrained conditions. After applying our rigorous data exclusion criteria, 74 neurons were included in the analysis (see Materials and Methods; Fig. 2). This is a very large number of neurons compared to other head-unrestrained studies (e.g., Freedman and Sparks 1997; Knight, 2012). However, it is not large compared to some head-restrained studies, so we limited our analysis to data that showed significant spatial tuning, and limit our conclusions to the statistically significant neural population results described below.

As described in the Materials and Methods, our preliminary data analysis corroborated the findings of the previous study (Sajad et al., 2015), i.e. that target-relative to initial eye orientation (*T*) provided a significantly preferred fit for the full population visual response and future gaze position relative to initial eye orientation (*G*) provided the best overall fit for the full population motor response. We henceforth focus on the temporal transition along the *T*-*G* spatial continuum between these two events.

Figure 4*A* shows the activity profile of a typical neuron with visual, sustained delay, and movement responses using the standard conventions of aligning activity with either the onset of the visual stimulus (left panel) or the onset of the gaze shift (right panel). Figure 4*B* shows the time-normalized spike density plot corresponding to the raster and spike density plots in Figure 4*A*. The RF maps obtained at four representative time-steps (C1-C4) from these data are also shown. This neuron had a very sharp (small) and spatially-distinct (bound) visual RF (C1), and a similar movement RF (C4). The delay-related

activity (C2, C3) exhibited similar spatial tuning, but the RF was more constricted and less spatially organized. After applying our *T*-*G* continuum analysis we observed a progressive shift of the best-fit model from *T* part-way toward *G* (shown by red icons above the RF plots in Fig. 4*C*) as activity progressed in time. This trend was often observed in our preliminary analysis and thus prompted the population analyses that follow.

Mixed Population Analysis

Figure 4*D* shows the mean, time-normalized spike density profiles of the 74 neurons that qualified for our analysis (see Materials and Methods). This reveals the typical visual response (present in 52/74 neurons), followed by activity that was statistically significant during some or all of the delay period (present in 51/74 neurons), and the typical movement response (present in 64/74 neurons) of the FEF. For our model-fitting procedure, we sampled this data through 16 half-overlapping time-steps (see Materials and Methods). The activity at each time-step was first tested for spatial tuning and then the spatial code (i.e., best-fit model) was included if the test was positive. At least 50% of neurons were spatially selective at each time-step (see histograms in Fig. 4*E*, bottom panel).

The mean of the individual data points at each time-step (○ ±SEM) as well as the fits made to each neuron's data points (black line) for spatially-selective responses at every time-step is shown in Figure 4*E* (The median was nearly identical in this dataset, not shown). Importantly, this method of illustrating the data (which we will use henceforth) provides the full spatiotemporal continuum of information coded by the population, by

showing best-fits along the *T-G* continuum as a function of our 16 time-steps through the normalized evolution of the trials. These data reveal that the overall population best-fit model started from a location near *T* and monotonically and almost linearly moved towards *G* as activity evolved from dominantly vision related – through the delay activity – to movement related (R_s = 0.90, p = 2.44 × 10^{-6}, Spearman's ρ correlation) . On average, for the spatially-tuned responses the best-fit intermediate *T-G* model explained 21% of the variance in the early visual activity (1st time-step), while it decreased to approximately 12-13% during mid-delay (7-9th time-steps), and 23 % in the peri-saccadic movement period (15th time-step). Since these results were better than any of the other comprehensive list of spatial models we tested, this unaccounted variance was presumably due to non-spatial factors such as attention, motivation, and random noise.

The *T*-to-*G* progression is not due to temporal smoothing of responses between the visual-memory transition and memory-motor transition (Figure 3B), because similar trends and statistics were observed when the visual and motor responses were removed entirely from the analysis (this is illustrated for VM neurons with sustained delay activity in Fig. 8). Framed in terms of our model-fitting method, these results mean that the population activity is initially unrelated to future gaze position errors, but as the memory interval progresses, these variable gaze errors are increasingly reflected within the population code. Separate analysis of shorter vs. longer memory intervals (not shown) yielded no difference in the results.

To examine the contribution of different cell types to this progression in spatial coding, we subdivided our population into four subpopulations, based on whether or not they

had visually-evoked, delay-, or movement-related activities (see below, and Materials and Methods) and performed the same analysis for each sub-population (Bruce and Goldberg, 1985).

Neurons with Visual Responses (Visual and Visuomovement Neurons)

Our population of neurons with visual responses was further divided into two classes based on whether or not they also exhibited movement activity (see Materials and Methods for quantitative definitions of each neuron class). In total, we had 10 V neurons and 42 VM neurons. For these neurons, activity was sampled through time from visual response onset until a post-saccadic period staring at the onset of the gaze movement, using only the epochs that tested positive for spatial tuning.

Visual neurons

Figure 5*A* shows the spike density profile (top panel) and model fits through time (bottom panel) for a typical V neuron, with a strong visual response but little or no delay or movement-related activity showing typical results. This neuron only exhibited spatial tuning (see Materials and Methods) at the first four time-steps. The RF plot (in the best-fit representation) corresponding to the first time-step, which corresponds to the early visual activity is shown in Figure 5*A* (bottom panel) showing that this visual neuron had a small and bounded RF with sharp spatial tuning. At all four time-steps the *T*-*G* continuum analysis provided fits near the *T* model (Fig. 5*A*, bottom panel). Most visual neurons showed a similar trend for *T* preference in the visual response, consistent with our previous results (Sajad et al., 2015). Figure 5*B* illustrates the corresponding analysis for the entire V neuron population, showing the mean spike density profile

(upper panel) and model fits through time using conventions similar to Figure 4*D* and 4E. Across the V population only the first three time-steps (corresponding to the visual transient response) exhibited significantly higher spatial coherence (lower fit residuals) than the pre-target period ($p < 0.05$; green colored data). Of the fits at these time-steps (green circles), the first were very near to *T*. The next two time-steps showed a trend to drift toward *G*, but none were significantly different from *T* ($p > 0.05$, One-sample Wilcoxon Signed-Rank Test). Although some V neurons showed declining activity during the delay period, this did not pass our population spatial tuning criteria (see Materials and Methods), and gave highly variable fits (gray shaded area) that were not further considered.

Visuomovement neurons

A similar analysis was performed on VM neurons. VM neurons were particularly of interest in this study because they exhibited both a visual and a movement response, and unlike V neurons, a large proportion of them exhibited delay activity (*n* = 36/42). Figure 6*A* (top panel) shows the time-normalized spike density plot for an example VM neuron with a large visual response followed by a delay response leading to a small movement response. This neuron exhibited significant spatial tuning at all 16 time-steps. The early visual response of this example was best described by intermediary models almost at the mid-point between *T* and *G*. However, from the third time-step onward, there was a monotonic change in the best-fit model from a model near *T* to a model near *G* (Fig. 6*A*, bottom panel). RF plots corresponding to the highlighted time-steps in panel A (bottom panel) are shown in panel C. Similar to the VM example shown in Figure 4*A*-*C*, although the RFs corresponding to the delay period is attenuated and

more spatially restricted compared to the visual and movement RFs, they cover the same relative spatial position, though the spatial model that best fits each is different. The change in spatial code from *T* to *G* was present in the majority of VM neurons with delay activity: of the neurons that showed delay activity, 29/36 showed a positive increment along the *T*-*G* continuum. However, the degree of this change was variable across neurons (mean +4.65 ± 6.47 Standard deviation in *T*-*G* units).

The monotonic (constant direction) change in spatial code from *T* to *G* was also observed at the population level in the VM neurons (n = 42) (Fig. 6*B*). Specifically, the mean population code in the first time-step (corresponding to early visual response) fell close to *T* (two steps towards *G* along the *T*-*G* continuum), but unlike V neurons it was significantly different from *T* ($p = 3.2 \times 10^{-5}$, One-sample Wilcoxon Signed-Rank Test). The mean population code then progressed monotonically (almost linearly) towards *G* ($R_s = 0.91$, $p = 9.08 \times 10^{-7}$, Spearman's ρ correlation). However, at the final time-step (corresponding to a period within the movement response and just after gaze onset), it was still significantly different from *G* ($p = 3.51 \times 10^{-7}$, One-sample Wilcoxon Signed-Rank Test; Fig. 6*B*, bottom panel).

Figure 7A illustrates how the distribution of best-fits for VM neurons evolves through time. Specifically, this histogram plots the best fit *T*-*G* distributions for the early-visual (step 1), early-delay (step 4), mid-delay (step 9), late-delay (step 13), and perimovement (step 15) intervals. Focusing on the delay activity (middle three panels), this population did not show a bimodal distribution of *T*-*G* with a diminishing *T* peak while *G* codes rose. Instead, during the delay, spatially tuned VM neurons showed a broad distribution of *T*-*G* codes that progressive shifted toward *G* (this shift is most

easily observed in the population means and medians, illustrated as vertical black and green lines).

To visualize how this occurs at the level of individual neurons, we plotted the delay *T*-*G* fits as a function of the motor *T*-*G* fits for each VM neuron that showed significant spatial tuning at all 5 time-steps (n=21). The top panel, corresponding to early-delay epoch, shows that the majority of the data points were shifted below the line of unity, toward the *T*-end of the distribution. Indeed, at this point in time the distribution is not significantly different from the visual distribution (0.3052, Paired-sample Wilcoxon Signed Rank Test). However, as the activity progresses through the mid- (middle panel) and late-delay (bottom panel) intervals the data points progressively migrate upwards, finally clustering more tightly around the motor code. At the late-delay interval, this difference is significantly different from the visual fits for the same population of neurons ($p = 0.0190$, Paired-sample Wilcoxon Signed Rank Test). When we further reduced this population to only those cells that showed significant spatial tuning at every single time-step of the delay (n=16), 13 of these neurons showed a positive slope in the *T*-to-*G* direction during the delay period (mean slope = 0.36 *T*-*G* units per time-step, SD = 0.52 *T*-*G* units per time-step).

Collectively the results reported above support the notion that in the VM population (and most individual VM neurons) the spatial code is not stable during the delay period but rather changes through the intermediate range between *T* and *G*, starting at a point closer to a target code and ending at a point closer to a gaze code.

584 To ensure that the *T-G* transition described above was not influenced by our time-
585 normalization procedure, or temporal blurring of spatial responses across different
586 epochs, we performed a more detailed technical analysis. For this technical analysis,
587 we used the best possible data we could obtain from our full dataset. First, we removed
588 any VM neurons that showed any temporal discontinuity during the delay, i.e., leaving
589 only those that showed sustained activity throughout the entire delay period (n = 22).
590 Then, we repeated our time-normalized analysis (Fig. 8*A*) on these data. This yielded
591 very similar trends and statistics to that observed for the overall population (linear
592 progressive trend in change from a code near *T* to a code near *G*; $R_s = 0.86$, $p = 2.40 \times$
593 10^{-5}, Spearman's ρ correlation).

594 Next, we performed a similar time-normalized analysis, but excluded the visual and
595 movement responses for every neuron (Fig. 8*B*). Once again a monotonic change in
596 spatial code with a significant slope ($R_s = 0.76$, $p = 0.0038$, Spearman's ρ correlation)
597 was observed. These results show that the progressive change in the spatial code
598 described above (Fig. 4, 6, 8*A*) is *not* due to the temporal smoothing of delay codes
599 with visual and movement responses.

600 Finally, we controlled for the possibility that the *T-G* transition might have been caused
601 by specific events within each trial, and that our time normalization technique might
602 have blurred these events through time to create an apparently progressive *T-G*
603 transition (see Materials and Methods, and Fig. 3*B*), Specifically, activity was aligned
604 with three major task events (Fig. 8*C*), namely, target onset (left panel), Go-signal
605 (middle panel), and movement onset (right panel). The target-aligned analysis (left
606 panel) was performed from 80ms after target onset until the earliest Go-signal. In this

period, (which was roughly equivalent for all trials for a given neuron irrespective of delay duration) the change in spatial code did not greatly contribute to the overall change in spatial code (Fig 8*C*, left panel). Notably, the spatial code (both mean of the individual data points and the mean of the fits) was stable both before and after Go-signal (Fig 8*C*, middle panel), suggesting that the change in spatial code was not prompted by this signal. The same observation held for gaze movement onset (Fig 8*C*, right panel). Collectively, these control results reinforce our main result; that the spatial code during memory period changes progressively across the entire delay interval, rather than discretely under the influence of specific task events.

Neurons with no visual response (Delay-Movement and Movement-only Neurons)

In our population, 22 neurons exhibited movement response but lacked visual response. This movement population was further classified into two classes: Movement neurons with activity starting at least 100ms before the appearance of the Go-signal were classified as DM neurons (n = 12) and those with activity only appearing after the Go-signal were classified as M neurons (n = 10) (see Materials and Methods). Since these neuron types lacked a visual response, the first time-step used for our spatial fits (Fig. 9, 10) started from a fixed time (80ms) after target onset.

Delay-Movement Neurons

Figure 9*A* shows the time-normalized spike density plot for a representative DM neuron, with activity beginning 150ms after target onset, sustaining through the delay period, and leading into a pre-saccadic buildup towards the peak just around the time of gaze onset. This neuron first showed a spatially-tuned response at the third time-step. The

RF plots corresponding to the 5th, 10th, and 15th (centered on gaze onset) time-steps are shown in Figure 9*C*. Although there was a sudden rise in firing rate at around the time of gaze shift, there was no major change in the spatial code of this neuron through time. Instead, throughout the delay and motor epochs the spatial code of this neuron remained intermediate between *T* and *G*. At the population level, spatial coherence of DM neurons became significantly higher than the pre-target period at the 4^{th} time-step and thereafter. At all these time-steps the spatial code remained at an intermediate position between *T* and *G*, and significantly different from both *T* ($p = 4.88 \times 10^{-4}$) and *G* ($p = 0.0015$), even during the movement response, just after gaze onset (i.e., final time-step) (One-sample Wilcoxon Signed-Rank Test) . There was no apparent trend for change in the DM fits during the delay period (Fig. 9*B*). Consistent with this, there was no significant correlation between spatial code and time-step ($R_s = 0.47$, $p = 0.20$, Spearman's ρ correlation).

Movement-only neurons

Figure 10*A* (top panel) shows the activity of an example M neuron with activity rising just before the onset of the gaze shift (about 120ms before saccade onset). This neuron only showed spatial tuning for four time-steps around the time of gaze onset, showing a spatial code tightly centered around *G* (Fig. 10*A*, bottom panel). The RF plot shown here corresponds to the time-step centered at gaze onset. For the M population only the three time-steps straddling gaze onset showed significantly higher coherence index than the pre-target period (with other time-steps shown in gray; Fig. 10*B*). In all the time-steps in the motor epoch population spatial code was very close to *G* (less than

651 one step short of *G* along *T-G* continuum) and was not significantly different from *G* (p >
652 0.25 for each time-step, One-sample Wilcoxon Signed-Rank Test).

653 **Summary of results and comparison of sub-populations**

654 Figure 11*A* summarizes and compares the results for each of the neuron sub-
655 populations described above, by superimposing their population means and confidence
656 intervals within a single normalized spatiotemporal continuum plot. Based on the
657 amount and coherence of activity in the sub-population results described above, we
658 have divided the neuronal responses into a visual epoch (first three time-steps), the
659 delay epoch (next 10 time-steps), and the motor epoch (final three time-steps,
660 straddling gaze onset). During the visual epoch, V neurons start with a code very close
661 to *T*, but tend to converge toward the VM code (V and VM were not significantly
662 different in their three shared time-steps). Both the VM and DM populations showed an
663 intermediate spatial code throughout the delay period, as described above. There was
664 no statistical difference between these two populations at any shared time-steps (p >
665 0.20, two-tailed Mann-Whitney *U* test) and the slopes of the regression lines to
666 individual data points (not shown) were not significantly different (p = 0.87, linear
667 regression comparison). However, as described above only VM neurons showed a
668 significant slope. The VM trend-line starts closer to *T*, crosses the DM line about
669 halfway through the delay epoch, and then ends up closer to (but still significantly
670 different from) *G*. In summary, only VM neurons showed a significantly positive *T-G*
671 slope, but all spatial coding along the *T-G* continuum during the visual and delay epochs
672 (in V, VM, and DM populations) was similar, and all three would have contributed to the
673 overall population code in these epochs.

674 The most striking difference between sub-populations occurs toward the end, during the
675 motor epoch. Although three sub-populations are active at this point, only one (M) is not
676 significantly different from *G*, and is significantly different from both the DM and VM
677 neuron fits ($p = 6.16 \times 10^{-5}$ and $p = 3.49 \times 10^{-5}$ respectively, Bonferroni-corrected two-
678 tailed Mann-Whitney *U* test; using data pooled across the three final time-steps roughly
679 corresponding to the motor epoch). We noted that VM neurons (but not DM neurons)
680 showed a noticeable peak in their *T*-*G* distribution falling between the *T*-*G* midpoint and
681 *G* (Figure 7a, bottom panel), and wondered if these neurons contributed more to the
682 motor output. However, when we repeated the preceding statistical comparison,
683 restricting the VM population to these more *G*-like codes (n = 27), the difference from M
684 neurons was still significant ($p = 0.0127$, two-tailed Mann-Whitney *U* test).

685 To summarize, the overall impression across all four populations is of a gradual shift in
686 coding from *T* (in the pure visual response) toward an intermediate *T*-*G* code (relayed
687 between the V, VM, and DM populations), with a final discrete shift in coding toward *G*
688 (i.e. a pure motor code) in the M population.

Discussion

This is the first study to describe the entire spatiotemporal sequence of visual-memory-motor transformations during head-unrestrained gaze shifts toward remembered visual stimuli. The current study was motivated by our previous study, which used a memory-delay task to show that 1) FEF visual activity codes target position (*T)* whereas 2) peri-saccadic motor activity codes future gaze position *(G)* (Sajad et al., 2015), but we did not show *when* or *how* this transition occurred. Further, we did not show how different cell populations contributed to this transition. Here, we addressed these questions by using a larger dataset (30% more neurons) and a new analytic method to track spatial coding along the *T-G* continuum through time. This resulted in two novel and important findings: 1) FEF delay activity (particularly in VM cells) showed a *progressive* evolution through intermediate *T-G* codes, and 2) an additional discrete jump occurred between intermediate *T-G* coding in the late delay / motor activity of VM and DM cells, to *G* coding in M-only cells during the final memory-motor transformation for saccades.

Our methodology combined several advantageous approaches: 1) head-unrestrained recordings (necessary to eliminate non-relevant spatial models in our preliminary analysis, and to provide the best behavioral estimate of frontal cortex output; Corneil et al., 2007; Paré et al., 1994; Martinez-Trujillo et al., 2003; Sajad et al, 2015), 2) a simple memory-delay saccade paradigm (avoiding the interpretive issues associated with sensory-motor dissociation tasks; Johnston et al., 2009; Hawkins et al., 2013), and 3) considering possibility for intermediate spatial codes rather than adhering to the traditional binary classification of the spatial code as sensory or motor (the significance of this will be further elaborated below). To our knowledge, this is the first time such a

712 combination of techniques has been applied to the FEF or any other brain area to
713 characterize the spatial codes in delay period. Although head-unrestrained recordings
714 were critical for narrowing down our analysis to *T* and *G* (and hence the intermediate *T-*
715 *G*) models, similar results would be expected in head-restrained conditions provided
716 that there is enough variability in behavior to adequately separate *T* and *G*.

717 **Intermediary codes in the delay period**

718 Several previous studies have proposed that spatial working memory evolves through
719 time from a sensory to motor code, when these are dissociated in some fashion
720 (Goldman-Rakic, 1987; Gnadt et al., 1991; Fuster, 2001; Postle, 2006). Consistent with
721 this, Takeda and Funahashi (2004) showed that the population spatial code in dlPFC
722 progressively rotates from a sensory vector to a motor vector during a memory delay, in
723 animals trained to rotate saccade direction relative to visual direction. Zhang and
724 Barash (2004) showed a reversal from 'pro' to 'anti' coding across LIP neurons in the
725 delay preceding anti-saccades. In the current study we found that FEF delay activity
726 showed a progressive transition from a *T* code that faithfully indicated target location,
727 through intermediate *T-G* codes that approached, but did not quite reach coding future
728 gaze position. This *T-G* progression was statistically significant at the neural population
729 level, and we observed similar trends in at least some neurons. This finding differs from
730 results of studies that spatially dissociated from the presented visual stimulus by virtue
731 of cognitive manipulations (such as rotation or reversal) of the sensory vector
732 (Funahashi, 1989, 1993; Takeda and Funahashi, 2002). In these studies, the
733 sensorimotor transition involved a progressive decrease of activity in visually-tuned cells
734 combined with a progressive increase of activity in motor-tuned cells (Takeda and

735 Funahashi, 2004, 2007; Zhang and Barash, 2004). We did not observe this in our
736 simpler memory-delay task, but rather a progressive change in coding along the *T-G*
737 continuum within the same population (i.e., VM neurons), even within neurons.

738 To our knowledge, only one other neurophysiological study has considered the change
739 in spatial code within one population of neurons during a memory delay. Wimmer et al.,
740 (2014) found that activity in the dlPFC showed increased correlations with variations in
741 final gaze position during a memory-delay period. Since the *T-G* transition observed in
742 our results signifies a progressively increased correlation of FEF delay activity with gaze
743 errors (discussed below), it resembles previous dlPFC results (Wimmer et al., 2014).
744 Similar results in FEF and dlPFC are in agreement with their reciprocal connectivity and
745 their close relationship in the maintenance of working memory (O'Sullivan et al., 1995;
746 Sweeney et al., 1996; Offen et al., 2010). Note that the main source of the *T-G*
747 progression within our full FEF population appeared to be VM neurons (Fig. 6-8). This
748 trend was statistically significant in VM neurons, whereas, DM neurons did not show a
749 statistically significant progression (Fig 9*B*). There is currently no clear consensus
750 whether both classes of neurons contribute to the psychological phenomenon of
751 working memory (Simon et al., 2002; Lawrence et al., 2005; Heinzle et al., 2007;
752 Sommer and Wurtz, 2001). However, a survey of previous publications suggests that
753 DM neurons might be more closely associated with motor planning, whereas VM
754 neurons may be more closely associated with mnemonic functions (Takeda and
755 Funahashi, 2007; Takaura et al., 2011; Markowitz et al., 2015). This notion is
756 consistent with findings that visually-responsive neurons are responsible for retaining
757 and updating visual memory in the superior colliculus (SC) (Sparks and Porter, 1983;

Dash et al., 2015). Alternatively, it may be that all delay-responsive neurons in the gaze network are connected through an internal feedback loop for working memory, and influence each other's spatiotemporal profiles (Verduzco-Flores et al., 2009; Okamoto et al., 2007; Curtis 2006).

Transformations between sensory, memory, and motor codes

The second novel observation in this study was the demonstration of discrete changes in the spatial code towards G, in the transition *between* visual, memory, and motor signals. Some theoretical studies have considered spatial transformations throughout this sequence of events (Brown et al., 2004; Faisal et al., 2008; Ma et al., 2014), and some experimental oculomotor studies have inferred from their data that additional memory-to-motor transformations must occur after the delay period (Stanford and Sparks, 1994; Opris et al., 2003). However, to our knowledge, these transformations have never been directly identified in neural signals. Here we have relied on the presumption that transformations between functional networks are inherently noisy (Alikhanian et al., 2015; Ma et al., 2014; Faisal et al., 2008) to infer the occurrence of transformations based on discrete accumulations of variable errors. Our data suggest that spatial transformations might occur upstream from VM neurons, because they already show a slightly shifted intermediate code at the start of the visual response. As described above, further transition of spatial code occurs during the memory delay, possibly due to degrading memory representations, but importantly, there is an additional transition from an intermediate *T-G* code in VM/DM neurons to a pure *G* code in M neurons at the end of the delay period (even when only compared VM vs. M neurons with preference for gaze-related models). To our knowledge, this is the first

781 direct demonstration of a memory-to-motor transformation between cells within the
782 same structure.

783 **Conceptual Model and Sources of Variable Error**

784 It is important to note that our model-fitting method relies on the relationship between
785 variability in neural firing rate and variability in behavior. In particular, the *T-G* continuum
786 reflects the degree to which neural firing rate faithfully represents target location for an
787 idealized saccade, versus the variable errors in actual future gaze direction. Thus, the
788 *T-G* scores shown in Figure 11*A* can be interpreted as reflecting the progression of
789 gaze error coding in different neural populations through time. With this in mind, Figure
790 11*B* schematically summarizes the possible flow of spatial signals within the FEF during
791 our task, and how these mechanisms might contribute to gaze variations.

792 According to this model, both V and VM neurons receive relatively unprocessed spatial
793 information about the location of the visual stimulus relative to the eye but VM neurons
794 receive additional inputs from V (and perhaps other areas) containing errors that tend to
795 shift the spatial code slightly further toward *G* along the *T-G* continuum. This spatial
796 information is then maintained within a working memory / planning network comprised
797 of VM and possibly DM neurons, as well as their extrinsic connections (Zelinsky and
798 Bisley, 2015). Here, the spatial representation in VM neurons shifts through
799 intermediary *T-G* codes throughout the delay period, presumably through the
800 accumulation of noise in a recurrent feedback network (Burak and Fiete, 2012; Compte
801 et al., 2000; Wang et al., 2015). Upon the presentation of the Go-signal, the retained
802 spatial information is then disinhibited, thus producing the motor response in VM and

DM neurons. At the same time, this code is relayed to the M neurons, involving an additional transformation, pushing the final motor code almost to *G*. This is consistent with the notion of noise arising in the transformation from memory to motor network (Zheng and Wilson, 2002; Alikhanian et al., 2015; Avery and Krichmar, 2015). These signals could then influence behavior through projections to the brainstem (Kunzle et al., 1976; Segraves, 1992). For example, we have observed similar noisy gaze-related signals in the motor responses of the SC (Sadeh et al., 2015).

Overall, these observations suggest that the noisy gaze signal that we observed in the overall motor response in our previous study (Sajad et al. 2015) is not the result of a random or general degradation of visual signals, but rather arises from different sources and different types of cells that relay different signals through different synaptic networks (Lawrence and Snyder, 2005; Chatham and Badre, 2015; Markowitz et al., 2015). To simple terms, our data support a combination of the gradual progression model and late transformation models illustrated in Figure 1*D*.

Behavioral and Clinical Implications

The noise-source model shown in Figure 11*B* could be useful for understanding and investigating behavior in both healthy and clinical populations. It is reasonable to assume that the sources of these variable errors would be vulnerable to diseases that affect frontal cortex function (Avery and Krichmar, 2015). If so, this confirms that analysis of variable errors in memory-delay saccade task has diagnostic value for diseases that affect frontal cortex function (Ploner et al., 1999). Further, whereas most behavioral studies interpret errors from memory delay tasks only in terms of

maintenance (e.g., Oyachi and Ohtsuka, 1995; D'Esposito and Postle, 1999; Wimmer et al., 2014) *or* transformations (e.g., Henriques et al., 1998; Vesia et al., 2010; Dessing et al., 2012), our study confirms that both maintenance and memory-to-motor transformations must be taken into account (Gnadt et al., 1991; Avery and Krichmar, 2015). For example, numerous clinical studies have considered errors that arise in working memory maintenance (Minshew et al., 1999; Sweeney et al., 2007; Mazhari et al., 2010), but there is also evidence that errors arise in the gating of memory signals to action in Parkinson's and Schizophrenic patients (Avery and Krichmar, 2015; Ketcham and Stelmach, 2003; Rottschy et al., 2013). Thus, the observed errors in these patients could be interpreted as degraded states of noisy memory and memory-to-motor transformations observed here.

References

Alikhanian H, de Carvalho SR, Blohm G (2015) Quantifying effects of stochasticity in reference frame transformations on posterior distributions. Front Comput Neurosci 9:82. doi: 10.3389/fncom.2015.00082.

Avery MC, Krichmar JL (2015) Improper activation of D1 and D2 receptors leads to excess noise in prefrontal cortex. Front Comput Neurosci. Doi:10.3389/fncom.2015.00031

Avillac M, Deneve S, Olivier E, Pouget A, Duhamel JR (2005) Reference frames for representing visual and tactile locations in parietal cortex. Nat Neurosci 8:941-949.

Bays PM, Gorgoraptis N, Wee N, Marshall L, Husain M (2011) Temporal dynamics of encoding, storage, and reallocation of visual working memory. J Vis 11(10) doi: 10.1167/11.10.6.

Blohm G, Keith GP, Crawford JD (2009) Decoding the cortical transformations for visually guided reaching in 3D space. Cereb Cortex 19(6):1372-1393

Bremner LR, Andersen RA (2014) Temporal analysis of reference frames in parietal cortex area 5d during reach planning. J Neurosci 34:5273-5284.

Brown JW, Bullock D, Grossberg S (2004) How laminar frontal cortex and basal ganglia circuits interact to control planned and reactive saccades. Neural Networks 17:471-510.

Bruce CJ, Goldberg ME (1985) Primate frontal eye fields. I. Single neurons discharging before saccades. J Neurophysiol 53:603-635.

857 Burak Y, Fiete IR (2012) Fundamental limits on persistent activity in networks of
858 noisy neurons. Proc Natl Acad Sci U S A 109:17645-17650.

859 Chatham CH, Badre D (2015) Multiple gates on working memory. Curr Opin Behav
860 Sci 1:23-31.

861 Compte A, Brunel N, Goldman-Rakic PS, Wang X-J (2000) Synaptic mechanisms
862 and network dynamics underlying spatial working memory in a cortical network
863 model. Cereb Cortex 10:910-923.

864 Constantinidis C, Franowicz MN, Goldman-Rakic PS (2001)The sensory nature of
865 mnemonic representation in the primate prefrontal cortex. Nat Neurosci 4:311-316.

866 Corneil BD, Munoz DP, Olivier E (2007). Priming of head premotor circuit during
867 oculomotor preparation. J Neurophysiol 97(1):701-714.

868 Crawford JD, Ceylan MZ, Klier EM, Guitton D (1999) Three-dimensional eye-head
869 coordination during gaze saccades in the primate. J Neurophysiol 81:1760-1782.

870 Curtis CE (2006) Prefrontal and parietal contributions to spatial working memory.
871 Neuroscience 139(1):173-180.

872 Curtis CE, D'Esposito M (2006) Selection and maintenance of saccade goals in the
873 human frontal eye fields. J Neurophysiol 95:3923-3927.

874 Dash S, Yan X, Wang H, Crawford JD (2015) Continuous updating of visuospatial
875 memory in superior colliculus during slow eye movements. Curr Biol 25:267-274.

876 De Bie J, Brink V, Van Sonderen J (1987) The systematic undershoot of saccades:
877 A localization or an occulomotor phenomenon? In: J.K. O'Regan and A. Levy-
878 Schoen, Editors, eye movements: From physiology to cognition, Elsevier, New York,
879 85/94.

880 DeSouza JFX, Keith GP, Yan X, Blohm G, Wang H, Crawford JD (2011) Intrinsic
881 reference frames of superior colliculus visuomotor receptive fields during head-
882 unrestrained gaze shifts. J Neurosci 31(50):18313-18326.

883 D'Esposito M, Postle BR (1999) The dependence of span and delayed-response
884 performance on prefrontal cortex. Neuropsychologia 37(11):1303-1315.

885 Dessing JC, Byrne PA, Abadeh A, Crawford JD (2012) Hand-related rather than
886 goal-related source of gaze-dependent errors in memory-guided reaching. J Vis
887 12(11). pii: 17. doi: 10.1167/12.11.17.

888 Dias EC, Segraves MA (1999) Muscimol-induced inactivation of monkey frontal eye
889 field: effects on visually and memory-guided saccades. J Neurophysiol 81:2191-
890 2214.

891 Everling S, Munoz DP (2000) Neuronal correlates of preparatory set associated with
892 pre-saccades and anti-saccades in the primate frontal eye field. J Neurosci
893 20(1):387-400.

894 Faisal AA, Selen LP, Wolpert DM (2008) Noise in the nervous system. Nat Rev
895 Neurosci 9:292-303.

Freedman EG, Sparks DL (1997) Activity of cells in the deeper layers of the superior colliculus of the rhesus monkey: evidence for gaze displacement command. J Neurophysiol 77(5):2328-2348

Funahashi S, Bruce CJ, Goldman-Rakic PS (1989) Mneumonic coding of visual space in the monkey's dorsolateral prefrontal cortex. J Neurophysiol 61(2):331-349.

Funahashi S, Chafee MV, Goldman-Rakic PS (1993) Prefrontal neuronal activity in rhesus monkeys performing delayed anti-saccade task. Nature 365:753-756.

Fuster JM (2001) The prefrontal cortex - an update: time is of the essence. Neuron 30:319-333.

Gaymard B, Ploner CJ, Rivaud-Pechoux S, Pierrot-Deseilligny C (1999) The frontal eye field is involved in spatial short-term memory but not in reflexive saccade inhibition. Exp Brain Res 129:288-301.

Gnadt JW, Andersen RA (1988) Memory related motor planning activity in posterior parietal cortex of macaque. Exp Brain Res 70:216-220.

Gnadt JW, Bracewell RM, Andersen RA (1991) Sensorimotor transformation during eye movements to remembered visual targets. Vision Res 34:93-106.

Goldman-Rakic PS (1987) Circuitry of primate prefrontal cortex and regulation of behavior by representational memory. In Handbook of Physiology – The Nervous System V, F. Plum and V. Mountcastle, eds. (Bethesda, Maryland: American Physiological Society), pp. 373–417.

916 Gottlieb J, Goldberg ME (1999) Activity of neurons in the lateral intraparietal area of
917 the monkey during an antisaccade task. Nat Neurosci 2:906-912

918 Hawkins KM, Sayegh P, Yan X, Crawford JD, Sergio LE (2013) Neural activity in
919 superior parietal cortex during rule-based visual-motor transformations. J Cogn
920 Neurosci 25(3):436-454.

921 Heinzle J, Hepp K, Martin KAC (2007) A microcircuit model of the frontal eye fields.
922 J Neurosci 27:9341-9353.

923 Henriques DY, Klier EM, Smith MA, Lowy D, Crawford JD (1998) Gaze-centered
924 remapping of remembered visual space in an open-loop pointing task. J Neurosci
925 18(4):1583-1594

926 Johnston K, DeSouza JF, Everling S (2009) Monkey prefrontal cortical pyramidal
927 and putative interneurons exhibit differential patterns of activity between prosaccade
928 and antisaccade tasks. J Neurosci 29(17):5516-5524.

929 Keith GP, DeSouza JF, Yan X, Wang H, Crawford JD (2009) A method for mapping
930 response fields and determining intrinsic reference frames of single-unit activity:
931 Applied to 3D head-unrestrained gaze shifts. J Neurosci Methods 180:171-184.

932 Ketcham CJ, Hodgson TL, Kennard C, Stelmach GE (2003) Memory-motor
933 transformations are impaired in Parkinson's disease. Exp Brain Res 149:30-39.

934 Knight TA (2012) Contribution of the frontal eye field to gaze shifts in the head-
935 unrestrained rhesus monkey: neuronal activity. Neuroscience 225:213-236.

936 Krappmann P (1998) Accuracy of visually and memory-guided antisaccades in man.
937 Vision Res 38:2979-2985.

938 Kunzle H, Akert K, Wurtz RH (1976) Projection of area 8 (frontal eye field) to
939 superior colliculus in the monkey. An autoratiographic study. Brain Res 117(3):487-
940 492.

941 Lawrence BM, White RL, Snyder LH (2005) Delay-period activity in visual,
942 visuomovement, and movement neurons in the frontal eye field. J
943 Neurophysiol 94:1498-1508.

944 Ma WJ, Husain M, Bays PM (2014) Changing concepts of working memory. Nat
945 Neurosci 17(3):347-356.

946 Markowitz DA, Curtis CE, Pesaran B (2015) Multiple component networks support
947 working memory in prefrontal cortex. Proc Natl Acad Sci U S A 112(35):11084-
948 11089.

949 Martinez-Trujillo JC, Klier EM, Wang H, Crawford JD (2003) Contribution of head
950 movement to gaze command coding in monkey frontal cortex and superior colliculus.
951 J Neurophysiol 90(4):2770-2776.

952 Mazhari S, Badcock JC, Waters FA, Dragović M, Badcock DR, Jablensky A (2010)
953 Impaired spatial working memory maintenance in schizophrenia involves both spatial
954 coordinates and spatial reference frames. Psychiatry Res 179(3):253-258.

955 Mazzoni P, Bracewell RM, Barash S, Andersen RA (1996) Motor intention activity in
956 the macaque's lateral intraparietal areas. I. Dissociation of motor plan from sensory
957 memory. J Neurophysiol 76:1439-1456.

958 Minshew NJ, Luna B, Sweeney JA (1999) Oculomotor evidence for neocortical
959 systems but not cerebellar dysfunction in autism. Neurology 52(5):917-922.

960 Monteon JA, Avillac M, Yan X, Wang H, Crawford JD (2012) Neural mechanisms for
961 predictive head movement strategies during sequential gaze shifts. J Neurophysiol
962 108(10):2689-707. doi: 10.1152/jn.00222.2012.

963 Monteon JA, Constantin AG, Wang H, Martinez-Trujillo J,Crawford JD (2010)
964 Electrical stimulation of the frontal eye fields in the head-free macaque evokes
965 kinematically normal 3D gaze shifts. J Neurophysiol 104(6):3462-75. doi:
966 10.1152/jn.01032.2009.

967 Monteon JA, Wang H, Martinez-Trujillo J, Crawford JD (2013) Frames of reference
968 for eye-head gaze shifts evoked during frontal eye field stimulation. Eur J Neurosci
969 37(11):1754-65. doi: 10.1111/ejn.12175.

970 Offen S, Gardner JL, Schluppeck D, Heeger DJ (2010) Differential roles for frontal
971 eye fields (FEFs) and intraparietal sulcus (IPS) in visual working memory and visual
972 attention. J Vis 10:1-14.

973 Okamoto H, Isomura Y, Takada M, Fukai T (2007) Temporal integration by
974 stochastic recurrent network dynamics with bimodal neurons. J Neurophysiol
975 97:3859-3867.

976 Opris I, Barborica A, Ferrera VP (2003) Comparison of performance on memory-
977 guided saccade and delayed spatial match-to-sample tasks in monkeys. Vision
978 Research 43:321-332.

979 O'Sullivan EP, Jenkins IH, Henderson L, Kennard C, Brooks DJ (1995) The
980 functional anatomy of remembered saccades - a PET study. Neuroreport 6:2141-
981 2144.

982 Oyachi H, Ohtsuka K (1995) Transcranial magnetic stimulation of the posterior
983 parietal cortex degrades accuracy of memory-guided saccades in humans. Invest
984 Ophthalmol Vis Sci 36(7):1441-1449.

985 Paré M, Crommelinck M, Guitton D (1994) Gaze shifts evoked by stimulation of the
986 superior colliculus in the head-free cat conform to the motor map but also depend on
987 stimulus strength and fixation activity. Exp Brain Res 101(1):123-139.

988 Ploner CJ, Rivaud-Péchoux S, Gaymard BM, Agid Y, Pierrot-Deseilligny C (1999)
989 Errors of memory-guided saccades in humans with lesions of the frontal eye field
990 and the dorsolateral prefrontal cortex. J Neurophysiol 82(2):1086-1090.

991 Postle BR (2006) Working memory as an emergent property of the mind brain.
992 Neuroscience 139:23-38.

993 Pouget A, Snyder LH (2000) Computational approaches to sensorimotor
994 transformations. Nat Neurosci 3:1192-1198.

995 Rainer G, Rao SC, Miller EK (1999) Prospective coding for objects in primate
996 prefrontal cortex. J Neurosci 19:5493-5505.

997 Rottschy C, Kleiman A, Dogan I, Langer R, Mirzazade S, Kronenbuerger M, Werner
998 C, Shah NJ, Schulz JB, Eickhoff SB, Reetz K (2013). Diminished activation of motor
999 working-memory networks in parkinson's disease. PLoS One 8(4):e61786. doi:
1000 10.137/journal.pone.0061786.

1001 Sadeh M, Sajad A, Wang H, Yan X, Crawford JD (2015) Spatial transformations
1002 between superior colliculus visual and motor response field during head-
1003 unrestrained gaze shifts. Eur J Neurosci. Doi: 10.1111/ejn.13093.

1004 Sajad A, Sadeh M, Keith GP, Yan X, Wang H, Crawford JD (2015) Visual–motor
1005 transformations within frontal eye fields during head-unrestrained gaze shifts in the
1006 monkey. Cereb Cortex 25:3932-3952.

1007 Sato TR, Schall JD (2003) Effects of stimulus-response compatibility on neural
1008 selection in frontal eye field. Neuron 38:637-648.

1009 Segraves MA (1992) Activity of monkey frontal eye field neurons projecting to
1010 oculomotor regions of the pons. J Neurophysiol 68(6):1967-1985.

1011 Schall JD (2015) Visuomotor functions in the frontal lobe. Annu Rev Vis Sci 1:469-
1012 498.

1013 Simon SR, Meunier M, Piettre L, Berardi AM, Segebarth CM, Boussaoud D (2002)
1014 Spatial attention and memory versus motor preparation: premotor cortex
1015 involvement as revealed by fMRI. J Neurophysiol 88:2047-2057.

1016 Sommer MA, Wurtz RH (2001) Frontal eye field sends delay activity related to
1017 movement, memory, and vision to the superior colliculus. J Neurophysiol 85:1673-
1018 1685.

1019 Sparks DL, Porter JD (1983) Spatial locatization of saccade targets. II. Activity of
1020 superior colliculus neurons preceding compensatory saccades. J Neurophysiol
1021 49:64-74.

1022 Stanford TR, Sparks DL (1994) Systematic errors for saccades to remembered
1023 targets: evidence for a dissociation between saccade metrics and activity in the
1024 superior colliculus. Vision Res 34:93-106.

1025 Sweeney JA, Mintun MA, Kwee S, Wiseman MB, Brown DL, Rosenberg DR, Carl JR
1026 (1996) Positron emission tomography study of voluntary saccadic eye movements
1027 and spatial working memory. J Neurophysiol 75(1):454-468.

1028 Sweeney JA, Luna B, Keedy SK, McDowell JE, Clementz BA (2007). fMRI studies of
1029 eye movement control: investigating the interaction of cognitive and sensorimotor
1030 brain systems. Neuroimage 36:T54-T60.

1031 Takaura K, Yoshida M, Isa T (2011) Neural substrate for spatial memory in the
1032 superior colliculus after damage to the primary visual cortex. J Neurosci. 31(11):
1033 4233-4241.

1034 Takeda K, Funahashi S (2002) Prefrontal task-related activity representing visual
1035 cue location or saccade direction in spatial working memory tasks. J Neurophysiol
1036 87:567–588.

1037 Takeda K, Funahashi S (2004) Population vector analysis of primate prefrontal
1038 activity during spatial working memory. Cereb Cortex 14:1328-1339.

1039 Takeda K, Funahashi S (2007) Relationship between prefrontal task-related activity
1040 and information flow during spatial working memory performance. Cortex 43(1):38-
1041 52.

1042 Verduzco-Flores S, Bodner M, Ermentrout B, Fuster JM, Zhou Y (2009) Working
1043 memory cells' behavior may be explained by cross-regional networks with synaptic
1044 facilitation. PLoS One 4(8):e6399. doi: 10.1371/journal.pone.0006399.

1045 Vesia M, Prime SL, Yan X, Sergio LE, Crawford JD (2010) Specificity of human
1046 parietal saccade and reach regions during transcranial magnetic stimulation. J
1047 Neurosci 30(39):13053-13065.

1048 Wang L, Li X, Hsiao SS, Lenz FA, Bodner M, Zhou YD, Fuster JM (2015).
1049 Differential roles of delay-period neural activity in the monkey dorsolateral prefrontal
1050 cortex in visual-haptic crossmodal working memory. Proc Natl Acad Sci U S A
1051 111(2):E214-219.

1052 Watanabe Y, Takeda K, Funahashi S (2009) Population vector analysis of primate
1053 mediodorsal thalamic activity during oculomotor delayed-response
1054 performance. Cereb Cortex 19:1313-1321.

1055 White JM, Sparks DL, Stanford TR (1994) Saccades to remembered target
1056 locations: an analysis of systematic and variable errors. Vision Res 34:79-92.

1057 Wimmer K, Nykamp DQ, Constantinidis C, Compte A (2014) Bump attractor
1058 dynamics in prefrontal cortex explains behavioral precision in spatial working
1059 memory. Nat Neurosci 17:431-439.

1060 Wurtz RH, Sommer MA, Paré M, Ferraina S (2001) Signal transformations from
1061 cerebral cortex to superior colliculus for the generation of saccades. Vision
1062 Res 41:3399-3412.

1063 Zelinsky GJ, Bisley JW (2015) The what, where, and why of priority maps and their
1064 interactions with visual working memory. Ann N Y Acad Sci 1339:154-164.

1065 Zhang M, Barash S (2004) Persistent LIP activity in memory antisaccades: Working
1066 memory for a sensorimotor transformation. J Neurophysiol 91:1424-1441.

1067 Zheng T, Wilson CJ (2002) Corticostriatal combinatorics: The implications of
1068 corticostriatal axonal arborizations. J Neurophysiol 87:1007-1017.

Figure 1. An overview of the experimental paradigm and a conceptual schematic of the possible coding schemes in the FEF. A) Activity was recorded from single neurons in the FEF while monkeys performed memory-guided gaze task with the head free to move. Monkeys initially fixated a visual stimulus (black dot labeled F) for 400-500ms. A visual stimulus (black dot labeled *T*) was then briefly flashed on the screen for 80-100ms (left panel). After an instructed delay (variable in duration; 450-850ms or 700-1500ms) the animal made a gaze shift to the remembered location of the target (gray dot labeled *T*) upon the presentation of the Go-signal. The Go-signal was the disappearance of the initial fixation target (gray dot labeled F). Inaccuracies in behavior were tolerated such that if final gaze landed within a window around the target a juice reward was provided. B) Five gaze trajectories to a single target (black circle) within a wide array of target (5 × 7 for this example session; gray dots) within the neuron's approximate RF location are shown. Initial fixation positions (tail of the trajectory) were randomly varied within a central zone (large gray circle) on a trial-by-trial basis. Final gaze positions (white circles) fell at variable positions around the target. Variability in initial and final positions (relative to different frames of reference) of target, gaze (i.e., eye in space), eye (in head), and head was used to spatially differentiate sensory and various motor parameters in various frames of reference. We exploited the variability in behavioral errors to differentiate between spatial models based on target position (*T*) and final gaze position (*G*). C) Additionally, a continuum of intermediary spatial models spanning *T* and *G* were constructed to treat spatial code as a continuous variable; this allowed us to trace changes in spatial code as activity evolved from vision to memory delay,

during memory delay, and from memory delay to motor. D) shows some plausible schemes for the spatiotemporal evolution of neuronal code based on proposed theories: 1) The target code could be transformed into a gaze code early-on, and this gaze code maintained during memory (motor theory; light gray line), 2) the target code could be maintained in the memory (sensory theory; black line) and subsequently transformed into a gaze code upon movement initiation, or 3) the spatial code could gradually change from a target code to a gaze code (dark gray line).

Figure 2. Approximate location of the FEF, the recorded sites in the two monkeys and population results corresponding to each. A) shows the anatomical location of the FEF, located at the anterior bank of the arcuate sulcus. B) Sites within the FEF from which neurons were recorded in each animal are plotted (circles) in the coordinates of the recording chamber with the center (0,0) approximately located at the stereotaxic coordinates corresponding to the FEF (see Materials and Methods). The black semi-circle represents the edge of the recording chamber. The color code represents the neuron type recorded from each site. Low-threshold microstimulation at these sites evoked saccades ranging from 2 degrees (at the most lateral sites) and 25 degrees (at the most medial sites) in head-restrained conditions (Bruce and Goldberg, 1985).

Figure 3. An overview of the analysis methods for identifying spatial code and sampling neuronal activity from time-normalized activity profile. ***A,*** shows an example analysis for identifying the spatial code. Here, activity from early visual response (80-180ms after target onset) was sampled for analysis (***A-1***). ***A-2,*** shows the *T*-*G* continuum and three example RF-plots are shown for the visual response corresponding to the demarked models (arrows) along the *T*-*G* continuum. *T* is the eye-centered target model and *G* is the eye-centered gaze model. In the RF plots each circle represents firing rate data (diameter) for a single trial, plotted over position data corresponding to the tested model (in this study models spanning target model, *T*, and gaze model, *G*). The PRESS residuals are shown at the bottom of each RF plot. In each RF plot, the color code (blue-red scale corresponding to low-to-high) represents the non-parametric fit made to all data points. ***A-3,*** shows mean PRESS (y-axis) as a function of tested spatial model along the *T*-*G* continuum (x-axis). For this example visual response the best-fit model or spatial code (lowest PRESS residuals) is the intermediate model one step away from *T* (towards *G*). Although ***A*** shows analysis only for a single sampling window, for the main analyses reported in this study we sampled activity at 16 time-steps from visual response onset until gaze movement onset. For this we normalized the time between visual response onset until movement onset so we could collapse all trials together for analysis. ***B,*** shows the raster and spike density plots corresponding to the classic visually- (***B-1***) and movement- (***B-2***) aligned neuronal responses as well as the time-normalized spike density (***B-3***), and illustrates activity sampling based on each of these scheme

Figure 4. A representative neuron with visual, delay, and movement responses, and results for the overall population. ***A,*** shows the visual- (left) and movement- (right) aligned raster and spike density plots for a VM neuron with sustained delay activity. The visual response of this neuron is from 65-300ms after target onset and the movement response begins 30ms before gaze onset. ***B,*** shows the time-normalized activity profile corresponding to ***A*** with the period between visual response (VR) onset and gaze movement onset normalized for all trials. ***C,*** show the RF maps for four time-steps (***C1*** - ***C4***) sampled from the time-normalized activity profile (***B,*** light red shades) with the blue-to-red color gradient representing low-to-high neuronal activity levels. The best-fit model (i.e., spatial code) at each of these time-steps is depicted by a red triangle placed on the *T-G* continuum (panels above the RF plots). For this neuron there was a progressive but partial shift (three steps out of 10) in spatial code towards *G*. ***D,*** depicts the time-normalized spike density for the entire population ($n = 74$) including neurons with either visual or movement response or both. Neurons with movement-related activity beginning at or after gaze onset are eliminated. ***E,*** shows the mean (± SEM) of spatially-tuned best-fits at 16 half-overlapping time-steps from an early visual period (visual response onset for visually-responsive neurons, and 80ms after target onset if neuron was not visually responsive) until gaze movement onset time. The solid line shows the mean of the fits made to individual neuron data highlighting the change in the population spatial code along *T-G* continuum as activity progresses from vision to movement. The histogram in the bottom panel shows the percentage of neurons that exhibited spatial tuning (y-axis) at a given time-step (x-axis).

Figure 5. Single neuron example and population results for visual (V) neurons. ***A*,** shows the time-normalized spike density profile for an example V neuron (top panel) and the data points corresponding to the spatially-tuned time-steps across 16 half-overlapping time-steps (bottom panel). The RF plot corresponding to the highlighted time-step (first time-step in pink) is shown with the spatial code highlighted above the plot. ***B,*** shows the population time-normalized post-stimulus time histogram (mean ±SEM) and the mean (±SEM) of the spatially-tuned data points at these time-steps across the V population. Colored data points (bottom panel) correspond to time-steps at which the population spatial coherence was significantly higher than the pre-target baseline and gray shades correspond to eliminated time-steps with spatial coherence indistinguishable from pre-target baseline. The histogram shows the percentage of neurons at each time-step that exhibited spatial tuning. The baseline firing rate is calculated based on average firing rate in 100ms pre-target period is shown by the solid horizontal lines in spike density plots (***A*** and ***B*** top panels). For reference, the approximate Visual, Delay, and Motor epochs are depicted at top of the panels.

Figure 6. Single neuron example and population results for visuomovement (VM) neurons. ***A*** and ***B***, same conventions as Figure 5. ***C***, The RF plots corresponding to time-steps with highlighted data points (green boarder circles) in ***A*** (bottom panel) are shown, with the spatial code along *T*-*G* continuum highlighted above each plot.

Figure 7. Distribution of best-fit models across the *T-G* continuum for VM population through 5 time-steps through visual, delay and movement responses. ***A***, shows the distribution of best-fits for VM neurons for early-visual (1st time-step from the time-normalized activity profile), early-delay (4th time-step), mid-delay (9th time-step), late-delay (13th time-step), and peri-movement (15th time-step) intervals. Only neurons with significant spatial tuning are considered. The number of neurons contributing to each distribution is indicated on each panel (the number in the brackets also includes best-fits outside of the presented range). ***B***, plots the best-fit model describing the activity during each of the delay intervals (y-axis), versus the best-fit model describing the perimovement activity (red dots). Here, only the 21 neurons that contributed to all five panels in ***A*** were plotted. Note the trend (from the early to mid to late delay periods) for the data points to migrate towards the line of unity, i.e. toward their movement fits.

Figure 8. Spatiotemporal progression of neuronal code in VM neurons with sustained delay activity. ***A,*** shows the results with time-normalized activity sampling including visual and movement response using the same conventions as Figure 5*B* (bottom panel). ***B,*** shows the results for only the delay period, with visual and movement responses excluded. Specifically, activity was sampled from 12 half-overlapping steps from the end of visual response (on average 266ms after target onset) until the beginning of the movement response (on average 85ms before gaze onset). This duration was on average 635ms. ***C,*** shows spatial code at fixed-times intervals relative to specific task events: target onset (left), the Go-signal (middle) and gaze onset (right). For target-aligned analysis (***C***, left panel), time from 80ms after target onset and the earliest Go-signal was divided into 8 half-overlapping steps, resulting in sampling window size fixed for any session but ranging between 80 and 150ms depending on whether the earliest Go-signal appeared 450ms or 750ms relative to target onset for that session. The Go-signal-aligned analysis (***C***, middle panel) was performed using 100ms half-overlapping windows starting 150ms before to 150ms after the Go-signal. The movement-aligned analysis (***C***, right panel) was performed using half-overlapping 100ms sampling windows starting from 150ms before to 150ms after gaze onset. Notice that although there is no change in spatial code triggered by specific task events, there is a progressive change in spatial code from *T* towards *G* as we move away from time of target presentation (left panel) to the time of gaze onset (right panel) in agreement with the trend seen in ***A*** and ***B***.

Figure 9. Single neuron example and population results for delay-movement (DM) neurons. ***A*** and ***B***, follow the same conventions as Figure 5. ***C,*** follows the same convention as Figure 6*C*. Since these neurons lacked a visual response neuronal activity sampling started from 80ms after target onset.

Figure 10. Single neuron example and population results for movement-only (M) neurons. Same conventions as Figure 5 are used. Since these neurons lacked a visual response neuronal activity sampling started from 80ms after target onset.

Figure 11. Summary of the data for different neuron types and a proposed model of the flow of spatial information within the FEF. ***A,*** shows the relationship between the spatiotemporal codes of V (green), VM (red), DM (blue) and M (magenta) neurons. Asterisks (*) denote significant differences between neuron subtypes. ***B,*** shows a schematic of the possible flow of information. Target location information enters the FEF (but may already have undergone some spatial processing in VM neurons). The spatial code is maintained in working memory (WM), but monotonically changes towards *G* due to memory-related (mem) processes. Upon the presentation of the Go-signal, the most recent memory of target location (i.e., movement goal) is relayed to the motor (mot) circuitry (comprised of M neurons) which in turn encodes the metrics of the eminent gaze shift (*G*).

Statistical Table:

	Analysis	Data structure	Statistical test	Power
a	Monotonicity test for spatiotemporal code - entire population	y = spatial code, x = time-step	Spearman's ρ correlation	Rs = 0.90, p = 2.44×10^{-6}
b	V population (1st time-step) code vs. T-code	Normality in V code distribution not assumed, n = 10	One-sample Wilcoxon Signed Rank Test	p > 0.05
c	VM population (1st time-step) code vs. T-code	Normality in V code distribution not assumed, n = 41	One-sample Wilcoxon Signed Rank Test	p = 3.2×10^{-5}
d	Monotonicity test for spatiotemporal code - VM population	y = spatial code, x = time-step	Spearman's ρ correlation	Rs = 0.91, p = 9.08×10^{-7}
e	VM population (final time-step) code vs. G-code	Normality in V code distribution not assumed, n = 40	One-sample Wilcoxon Signed Rank Test	p = 3.51×10^{-7}
f	Early-delay (time-step 4) code vs. visual response (time-step 1) code	Normality in VM code distribution not assumed, n = 21	Paired-Sample Wilcoxon Signed Rank Test	p = 0.302
g	Late-delay (time-step 13) code vs. visual response (time-step 1) code	Normality in VM code distribution not assumed, n = 21	Paired-Sample Wilcoxon Signed Rank Test	p = 0.0190
h	Figure 7B: early-, mid-, and late-delay (time-steps 4, 9, 13) code vs. movement response (time-step 15) code	Normality in VM code distribution not assumed, n = 21	BonFerroni corrected; Wilcoxon test	p < 0.05 (see Fig 7B)
i	Monotonicity test for spatiotemporal code - VM neurons with sustained delay	y = spatial code, x = time-step	Spearman's ρ correlation	Rs = 0.86, p = 2.40×10^{-5}
j	Monotonicity test for spatiotemporal code (during delay-only period) - VM neurons with sustained delay	y = spatial code, x = time-step	Spearman's ρ correlation	Rs = 0.76, p = 0.0038
k	DM population (final time-step) code vs. T-code	Normality in DM code distribution not assumed	One-sample Wilcoxon Signed Rank Test	p = 4.88×10^{-4}
l	DM population (final time-step) code vs. G-code	Normality in DM code distribution not assumed	One-sample Wilcoxon Signed Rank Test	p = 0.0015
m	Monotonicity test for spatiotemporal code - DM population	y = spatial code, x = time-step	Spearman's ρ correlation	Rs = 0.47, p = 0.20
n	M population (final time-steps) code vs. G-code	Normality in M code distribution not assumed, n < = 10	One-sample Wilcoxon Signed Rank Test	p > 0.20

o	DM population vs. VM population code	Normality in neither population distribution is assumed	Mann-Whitney *U* test	p > 0.25 for each time-step
p	DM population vs. VM population spatiotemporal progression	Two slopes obtained from: y = spatial code, x = time-step	Linear regression comparison	p = 0.87
q1	VM population (motor epoch) vs. M population (motor epoch) code	Normality in neither population distribution is assumed	Bonferroni-corrected Mann-Whitney *U* test	$p = 6.16 \times 10^{-5}$
q2	DM population (motor epoch) vs. M population (motor epoch) code	Normality in neither population distribution is assumed	Bonferroni-corrected Mann-Whitney *U* test	$p = 3.49 \times 10^{-5}$
r	VM population (15th time-step) code vs. M neurons (15th time-step) but only neurons with preference for G-like codes	Normality in neither population distribution is assumed	Mann-Whitney *U* test	p = 0.0127

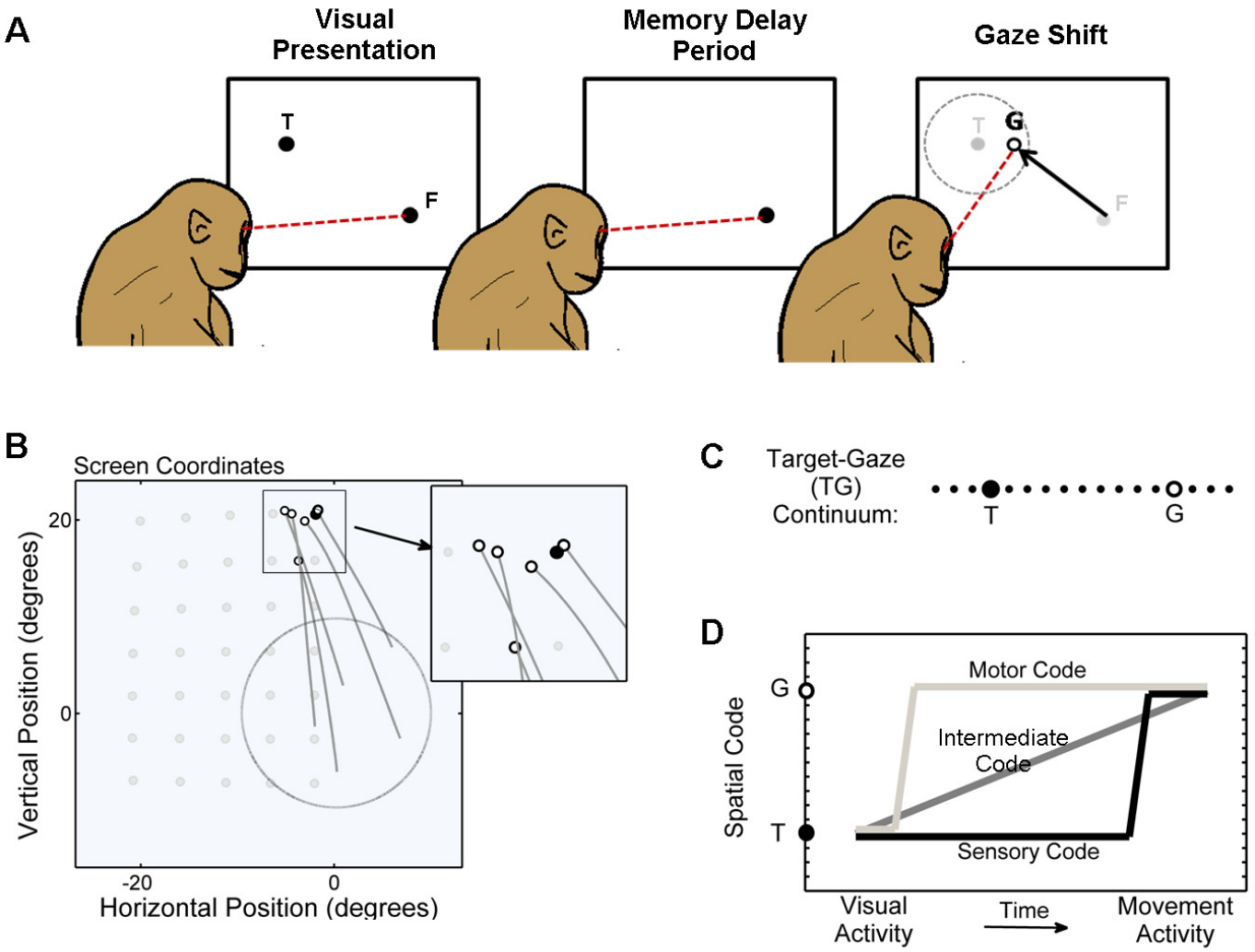

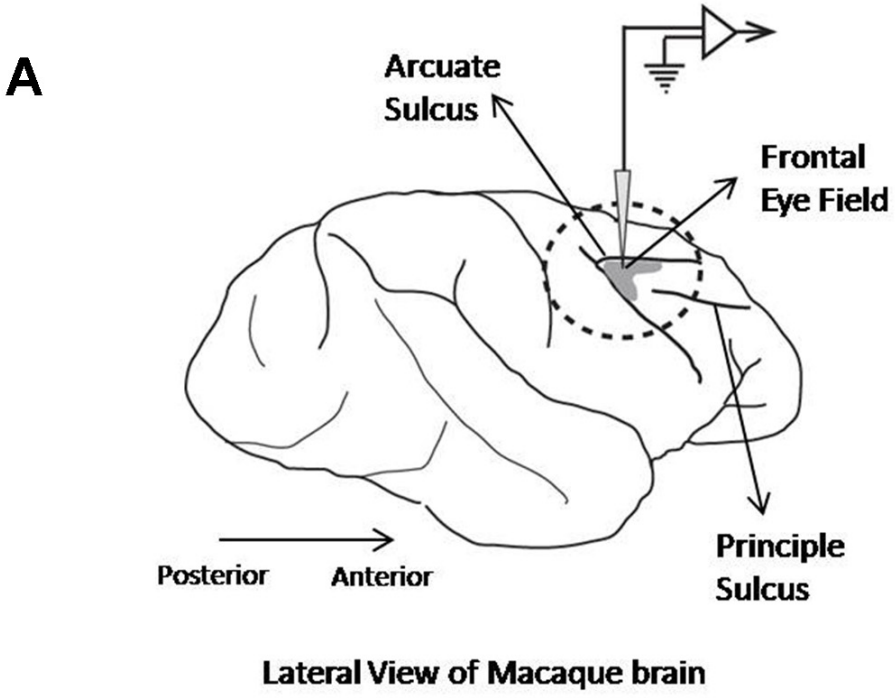

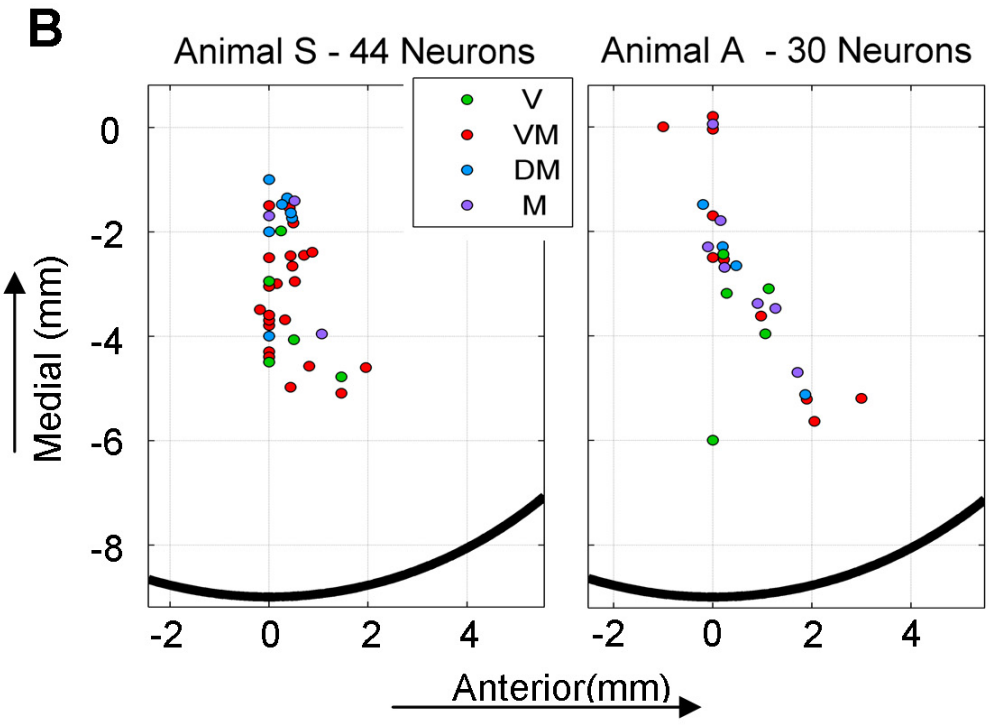

A) Spatial Analysis Method

A-1) Sampled Activity

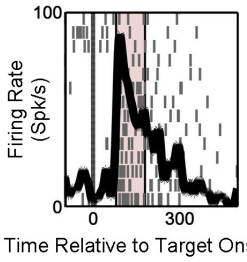

A-3) Identifying the Spatial Code

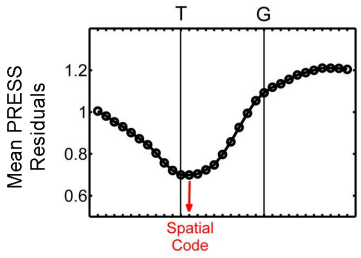

A-2) Tested Spatial Models: Target-Gaze Continuum

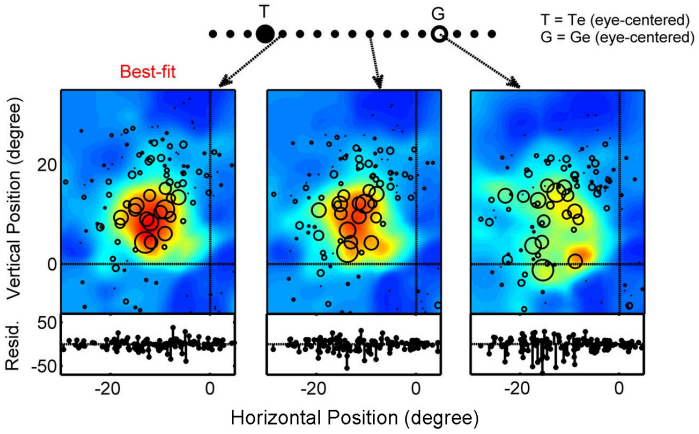

B) Time normalization and activity sampling

B-1) Visual Alignment of Neuronal Response

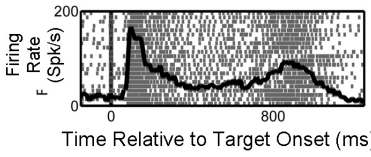

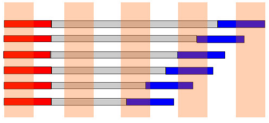

B-2) Movement Onset Alignment of Neuronal Response

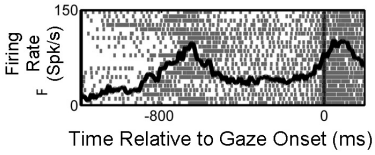

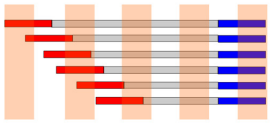

B-3) Time-Normalized Spike Density